IET Journals
The Institution of Engineering and Technology

GNSS based Passive UAV Monitoring: Feasibility Study

ISSN 1751-8644
doi: 0000000000
www.ietdl.org

Christos Ilioudis[1], *Carmine Clemente*[1], *John Soraghan*[1]

[1] *Electronic and Electrical Engineering, University of Strathclyde, 204 George St, Glasgow, UK*
** E-mail: c.ilioudis@strath.ac.uk*

Abstract: As unmanned aerial vehicles (UAVs) are becoming more accessible and easier to use, the need for a reliable and easy to deploy monitoring solution has become the subject of great importance in defence, security and commercial sectors. In this work, a novel passive bistatic radar is proposed to facilitate UAV detection and localisation by exploiting Global Navigation Satellite Systems (GNSS) as illuminators of opportunity (IO). The result of a feasibility study conducted to determine the maximum operational range of the system under different configurations as well as its parameter estimation capabilities were evaluated through simulations. To facilitate multiple satellites signals, a multiple-input single-output (MISO) approach is adapted to estimate the target's location and velocity.

1 Introduction

Based on their illuminators, radar systems can be categorised as active or passive [1]. Active systems utilise one or more dedicated transmitters with known and in many cases controlled operating parameters, such as carrier frequency and waveform. On the other hand, passive systems exploit illuminators of opportunity (IO) with limited knowledge and no control over them. Furthermore, depending on the relative distance between the transmitter and receiver, radar systems can be categorised as monostatic or bistatic. In recent years, passive bistatic radar (PBR) systems have been widely suggested for a variety of applications [2–11]. While having more limitations compared to their active counterparts, PBR systems offer an attractive monitoring solution especially for low cost and low size, weight and power (SWaP) applications as they exhibit lower manufacturing and operational cost as well as SWaP requirements due to the lack of emitting elements. Furthermore, since PBR do not transmit any signals, they do not require frequency allocation and cannot be detected through Radio-Frequency (RF) sensing systems making them harder to avoid and jam.

Due to the rising number of civilian and commercial unmanned aerial vehicles (UAV), a significant interest has been expressed on PBR architectures for UAV monitoring [2–4, 12, 13]. Particularly, in [12] a software defined 3G PBR was demonstrated highlighting the ability of the system to extract Doppler signatures of UAV targets. In [13], a PBR utilising a Digital Video Broadcasting-Terrestrial (DVB-T) IO was experimentally validated for UAV target detection and micro-Doppler signature extraction in distances of 250m. The authors in [2], also employed DVB IOs demonstrating the capability of the proposed system to detect and track UAV targets. A digital audio broadcasting (DAB) based PBR was proposed in [3] demonstrating the ability of the system to detect UAV targets up to a distance of 1.2km. Furthermore, in [4] mobile communication IOs were suggested, achieving detectable ranges of up to 300 and 150m for two different targets. While such approaches offer acceptable performance for some applications, they can only be applied in specific areas where the IOs offer good coverage. Global Navigation Satellite Systems (GNSS) IOs is an attractive solution as such systems offer persistent global coverage. In the literature, various GNSS based PBR systems have been proposed employing either spaceborne or earth-based receivers. In [14] and [15], the authors investigated the applications of GNSS spaceborne PBR in ocean reflectometry scenarios. An earth-based GNSS PBR was proposed in [10] for synthetic aperture radar (SAR) applications using a synchronization algorithm to generate the reference, satellite, signal at the receiver. In a similar approach, the authors in [11] proposed and experimentally validated a GNSS PBR system design for maritime target detection. A link budget study for airborne targets detection using GPS PBR was held in [16], where the shortcomings of such systems due to the high direct signal and clutter returns were highlighted.

Forward scattering (FS) is a special PBR configuration that occurs when the target crosses (or is very close to) the line of sight between the IO and the passive receiver. Depending on the dimension of the target relative to the operating signal's wavelength, an enhancement of the radar cross section (RCS) of the target can occur. For this reason, FS radar can be particularly attractive for targets with low reflectivity, as their FS-RCS is mainly dependent on the silhouette of the target and not by its material. Recently, FS radar systems have gained traction in the research community. Namely, in [5] and [6] the authors investigated and later validated in [7] the capability of a GNSS PBR system to extract micro-Doppler signatures of helicopter targets when operating in near FS configuration. In [8] the Doppler information extraction in a GNSS based FS was validated, while the authors in [9, 17] suggested a filter bank based algorithm that is able to estimate range and velocity parameters of a moving target. The closed form expression of the Cramér-Rao lower bound for target motion parameters estimation in FS was derived [18], while the feasibility of FS radars was validated through simulation analysis and experimental results.

In previous work, the concept of GNSS based PBR for UAV monitoring was investigated for FS configuration [19]. Specifically, a link budget analysis was conducted to determine the maximum detectable range of different size targets exploiting GPS and Galileo constellations. Furthermore, a GNSS PBR system design was proposed and implemented using a Software Defined Radio (SDR). Experimental acquisitions validated the feasibility of the system, while the application of Short Time Fractional Fourier Transforms (STFrFT) was also proposed to enhance the target parameter estimation capabilities. This paper extends the work held in [19] by considering both forward and back scattering RCS as well as exploiting multi-satellite acquisitions in a multiple-input single-output (MISO) configuration. The contribution of this work can be summarised as follows: extension of the proposed system for multi-satellite acquisition; evaluation of the maximum detectable range accounting BS and FS configurations, and time and multi-satellite integration; evaluation of the localisation capabilities in a MISO parameter estimation approach; investigation of micro-Doppler signatures in GNSS PBR configurations.

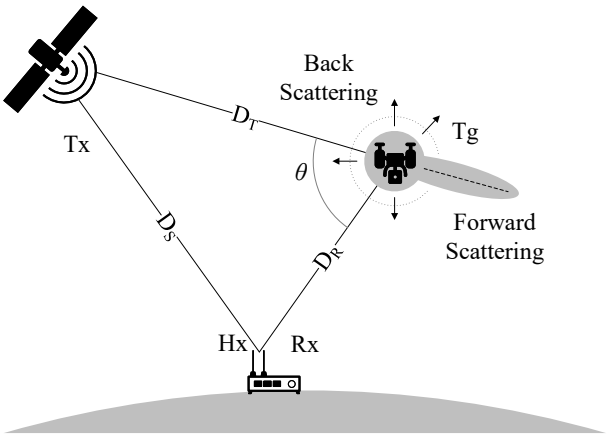

Fig. 1: Examined passive GNSS radar topology comprising a satellite IO Tx, a UAV target Tg, and a two channel receiver Hx and Rx.

The remainder of the paper is structured as follows. In Section 2 a link budget analysis is described that evaluates the maximum detectable range of low RCS targets under FS and BS configurations for different case studies. The proposed system design is described in Section 3 where a general GNSS signal model is derived along with the appropriate reconstruction algorithm. Section 4 discusses the proposed MISO target parameter estimation approach with the localisation performance of the system being also evaluated. The capability of the proposed system to discriminate between different micro-Doppler signatures is discussed in Section 5. Lastly, Section 6 concludes the paper.

2 GNSS availability and Detection Range

By definition, PBR systems can only operate under the presence of IOs as they do not comprise dedicated illuminators. The main drawback of using such an approach is that the overall performance of the system is highly dependent on the IOs operational characteristics. This becomes even more apparent when non-stationary IOs are taken into account. Particularly, for GNSS IOs the position and availability of illuminators shall be considered to assess the performance of the system. In this section the two GNSS constellations, Global Positioning System (GPS) and Galileo, are examined to assess their availability and maximum detectable range that they can offer for UAV targets.

2.1 Back and Forward Scattering

The examined system topology is illustrated in Fig. 1. The configuration comprises a satellite IO Tx, a ground passive receiver with two channels Hx and Rx, and an airborne target Tg, with their distances being denoted as: D_S satellite to receiver, D_T satellite to target, and D_R target to receiver. Initially the signal is emitted from the satellite to earth. A portion of it is directly received by Hx while another part first reaches Tg and is then scattered at different directions. Depending on the geometry, the passive receiver Rx will capture the echoes from the target from different scattering directions. Particularly, based on the bistatic angle θ, three distinct radar cross section (RCS) regions are distinguished: pseudo-monostatic BS at $\theta < 20^\circ$, BS at $20^\circ < \theta < 140^\circ$, and FS at $\theta > 140^\circ$. Compared to the other RCS regions, FS does not offer target ranging, however it can significantly increase the target's RCS in the forward direction [20].

The BS-RCS for miniature UAV targets has been widely discussed in [21, 22]. As the BS-RCS of such complex targets is hard to be estimated for every bistatic angle and target orientation, in this work the BS-RCS is modelled by the RCS of a sphere:

$$\sigma_{\mathrm{BS}} = \pi r^2 \tag{1}$$

where r is the radius of the sphere. As shown in [22], spheres with radius close to 8cm can well approximate the BS-RCS of a Parrot drone target at the 2.4GHz WiFi band. An overview of the FS-RCS phenomenology is provided in [23], while its applicability for miniature UAV detection was investigated in [19]. The maximum FS-RCS in the optical region can be calculated from [24]:

$$\sigma_{\mathrm{FS,max}} = 4\pi A^2/\lambda^2 \tag{2}$$

where A is the physical area of the target. This maximum value can only be observed if the receiver antenna falls into the forward scattering main lobe which is centred across the line of site between the transmitter and target facing the opposite direction from the transmitter, see Fig. 1, while its width is proportional to λ and inversely proportional to the target's typical dimension [23].

2.2 Link Budget Model

One of the main objectives of this analysis is to assess the maximum range the proposed GNSS PBR is capable to detect a miniature UAV target. In order to get a coarse estimation of this maximum operational range, an investigation on the link budget of the system is performed. Similarly to [19], the considered figure of merit is the signal to noise ratio (SNR), which for a single pulse is [25]:

$$\rho = \left(\frac{P_{\mathcal{T}} G_{\mathcal{T}}}{4\pi D_{\mathcal{T}}^2}\right)\left(\frac{\sigma}{4\pi D_{\mathcal{R}}^2}\right)\left(\frac{\lambda^2 G_{\mathcal{R}} L_s}{4\pi}\right)\frac{G_{\mathcal{P}}}{P_n} \tag{3}$$

where the different parameters are described in Table 1 along with their typical values derived from [19, 26]. It should be noted that the processing gain is calculated as the time bandwidth product of the signal, i.e. $G_{\mathcal{P}} = T \times B_s$. Additionally, as GNSS satellites operate in a Continuous Waveform (CW) manner, when referring to a single pulse the duration of a single code sequence transmitted by the satellite is assumed. To enhance the performance, coherent integration of duration T_I can also be considered, where the improved SNR is given as:

$$\hat{\rho} = \frac{T_I}{T}\rho \tag{4}$$

with T being the duration of the code used by the satellite. Furthermore, integration can also be achieved by using the returns of multiple satellites. Since the different satellites are expected to be widely distributed around the target, in most cases coherency between the different signals is not a realistic assumption and therefore non-coherent integration shall be considered. Non-coherent integration is less *efficient* than the coherent while its gain computation is also not straight forward. Assuming N non-coherent received signals, the SNR after integration is approximated as:

$$\tilde{\rho} = \sqrt{\sum_{i=1}^{N} \rho_i^2} \tag{5}$$

where ρ_i, $i = 1, 2, ..., N$ is the SNR achieved from each satellite.

Table 1 Satellite Link Budget Parameters

	Description		GPS	Galileo
λ	Wavelength	[cm]	19.03	19.03
$D_{\mathcal{T}}$	Satellite to target distance (mean)	[km]	20200	23222
$P_{\mathcal{T}}$	Transmitted power (mean)	[dBW]	21.7	23.9
$G_{\mathcal{T}}$	Transmitter gain (mean)	[dBi]	14.5	16.5
T	Code duration	[ms]	1	4
B_s	Code bandwidth	[MHz]	1.023	1.023
$G_{\mathcal{P}}$	Signal processing gain	[dB]	30.1	36.1
$G_{\mathcal{R}}$	Receiver gain	[dBi]	46	46
L_s	Losses	[dB]	-3	-3
P_n	Noise Power	[dB]	-128	-128
σ_{BS}	Target FS-RCS	[dBsm]	-17	-17
σ_{FS}	Target BS-RCS	[dBsm]	-4.65	-4.65
$\rho_{\min}$	Minimum SNR for detection	[dB]	8	8

Rearranging (3) it is possible to express the maximum detectable range for a certain set of configurations:

$$D_{\mathcal{R}} = \sqrt{\left(\frac{P_{\mathcal{T}} G_{\mathcal{T}}}{4\pi D_{\mathcal{T}}^2}\right)\left(\frac{\sigma}{4\pi\rho_{\min}}\right)\left(\frac{\lambda^2 G_{\mathcal{R}} L_s}{4\pi}\right)\frac{G_{\mathcal{P}}}{P_n}} \quad (6)$$

where $\rho_{\min}$ is the minimum SNR required for detection. Additionally, using (4) and (6) it can be easily shown that applying coherent processing the new detectable range can be expressed as:

$$\hat{D}_{\mathcal{R}} = \sqrt{\frac{T_I}{T}} D_{\mathcal{R}} \quad (7)$$

Moreover, in case of multiple satellites' integration, the maximum achievable range is approximated as:

$$\tilde{D}_{\mathcal{R}} = \sqrt[4]{\sum_{i=1}^{N} D_{\mathcal{R},\mathrm{i}}^4} \quad (8)$$

where $D_{\mathcal{R},\mathrm{i}}$ is the maximum achievable range using the i-th satellite. It is worth noting that certain variables in (6) and (7) can be parametrised in the system design process while others depend on the satellite properties and shall be considered constant. Particularly the transmitted power, gain, wavelength and processing gain have fixed values for each satellite. On the other hand, the receiver gain, ingratiation time, number of satellites and SNR for detection can be set in the system design. The rest of the parameters, such as the target RCS and noise power are unknown or cannot be controlled.

From Table 1 it can be seen that different constellations display different processing gain and code duration. This is due to each system using different codes and code bandwidths. Particularly, GPS has a code duration of 1ms while Galileo uses codes of 4ms. That is specifically important when coherent integration in time is considered as from (5) it can be derived that Galileo offers lower gain than GPS for the same T_I due to its longer pulse duration. This lower integration gain however is compensated by the higher processing gain Galileo's longer codes offer.

2.3 *Case Studies*

The link budget model described in Section 2.2 is applied to approximate the maximum distance that a miniature UAV target can be detected. As the GNSS coverage depends on the receiver's geographic position and will also vary in different parts of the day, the analysis is carried out for different locations of interest throughout a 24-hour period. The parameters used in this study are summarised in Table 1 while the individual satellites' power is provided by [26]. The satellite position model is based on the orbit computation method described in [27]. The method follows a modified version of the SGP4 model applied for standard satellite orbit computation using two-line elements (TLE). The position of each satellite is calculated for the full day (midnight to midnight) at 16/06/2019 based on the TLE files with same epoch date.

2.3.1 Case Study I: Heathrow Airport: The first examined case study is the Heathrow Airport, Longford TW6, London, UK. The location parameters of the receiver are set at 51.4700°N, 0.4543°W for latitude and longitude respectively, while the height is set at 25m above sea level. Initially each satellite is examined independently. The maximum detectable range achieved by each satellite, as calculated from (7) using BS-RCS and coherent integration of $T_I = 0.5$s, is shown in Fig.2. Particularly, Fig.2a and 2b show the maximum detectable range throughout one day for each satellite in the GPS and Galileo constellations respectively. Moreover, the last row indexed as "Max" shows the range when the satellite offering the maximum range at that part of the day is chosen. Also, zero range shown in grey colour indicates no satellite visibility. Comparing the results, it can be seen that while Galileo satellites can

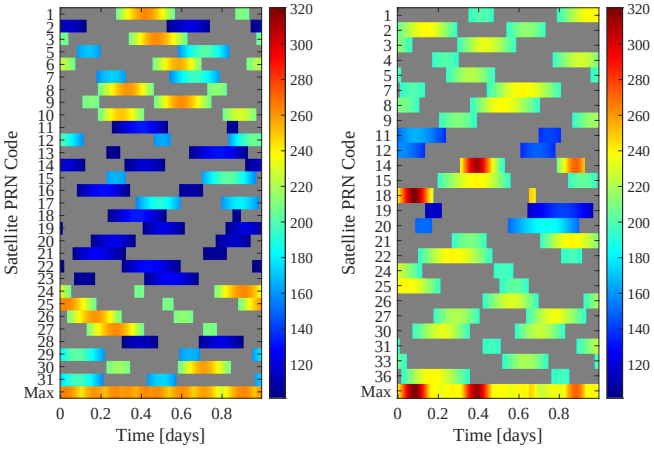

(a) GPS (b) Galileo

Fig. 2: Case Study I: Maximum detectable range [m] achieved in BS configuration using one satellite for detection.

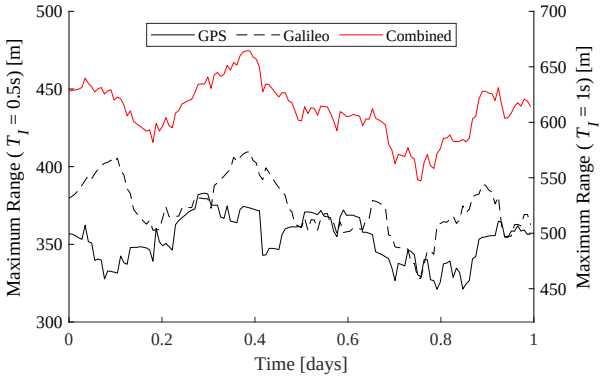

Fig. 3: Case Study I: Maximum detectable range achieved in BS configuration suing all the visible satellites in different constellations and a combination of both; left axis for integration time $T_I = 0.5$s and right axis for $T_I = 1$s.

offer higher detectable ranges than GPS, they do it for a small time window during the day.

To access the performance of the system when multiple satellites' signals are integrated, (8) is used. In Fig. 3 the maximum range offered is shown when all visible satellites in each constellation and a combination of both constellations are utilised. As it can be seen, the maximum achievable range after integrating multiple signal is significantly longer than what individual satellites offer. Moreover, the Galileo constellation offer higher detectable range for the most part of the day fluctuating between 330m and 410m for $T_I = 0.5$, see left axis in Fig. 3. Additionally, integrating all visible satellites from both constellations, significantly higher maximum detectable range varying from 390m up to 470m is achieved. These results can be further improved by increasing the integration time. As it can be seen from the right axis in Fig. 3 a maximum detectable range of 580m for Galileo and 660m for combined constellations is achieved.

As discussed in Section 2.1, the FS-RCS only occurs when the target is close to the baseline between the satellite illuminator and the ground receiver. For this reason, to access the performance of the system in such configuration only satellites positioned west of the airport, particularly between 160° and 200° azimuth angle, and between 5° and 50° elevation angle in topocentric coordinates system (TCS) are considered. In Fig. 4 the maximum detectable range achieved from each satellite in different constellations is shown

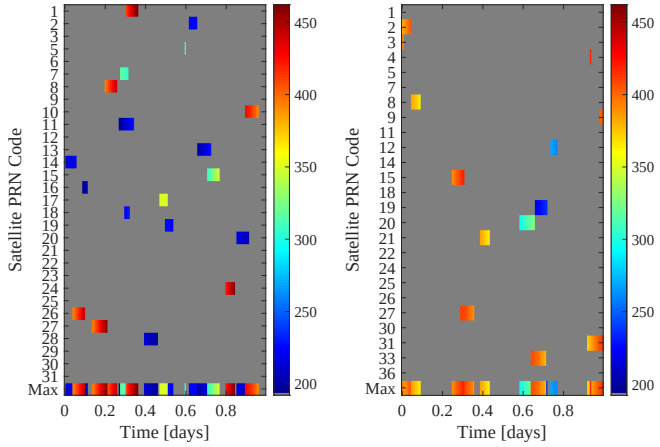

(a) GPS (b) Galileo

Fig. 4: Case Study I: Maximum detectable range [m] achieved in FS configuration using one satellite for detection.

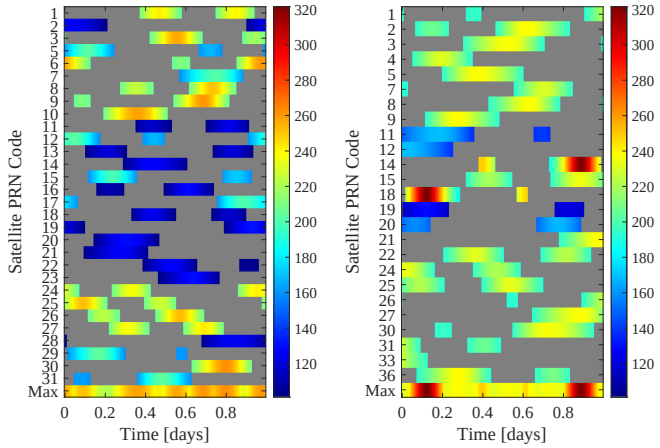

(a) GPS (b) Galileo

Fig. 5: Case Study II: Maximum detectable range [m] achieved in BS configuration using one satellite for detection.

using an integration time of $T_I = 0.1$s. Notice that T_I is significantly smaller when FS is considered due to the more restrictive topology. As it can be seen, the detectable range is longer compared to Fig. 2, even if the integration time is shorter, which is due to the FS-RCS being significantly higher than BS-RCS. As it can be seen GPS offers longer ranges compared to the Galileo, while also being less sparse. Particularly, GPS will have non-zero range at 79.2% of the day compared to Galileo 51.4%.

2.3.2 Case Study II: Newark Liberty International Airport:

The second case study is the Newark Liberty International Airport, NJ 07114, USA, located at 40.6895°N, 74.1745°W for latitude and longitude respectively with the height being set at 25m above sea level. Similar to Case Study I the maximum detectable range achieved by individual satellites and by the integrating different signals are shown in Fig. 5 and Fig. 6 respectively. Comparing with the respective results in Case study I and II it can be seen that the satellite availability profiles appear different. This is expected as the receiver in the Case study II is placed in different geographical location than Case Study I. Moreover, comparing Fig. 2 with Fig. 5 it can be seen that the maximum range of the individual satellites is similar for both case studies. Furthermore, comparing Fig. 3 with Fig. 6, it can be seen that for the Case Study II the maximum detection ranges have generally lower values.

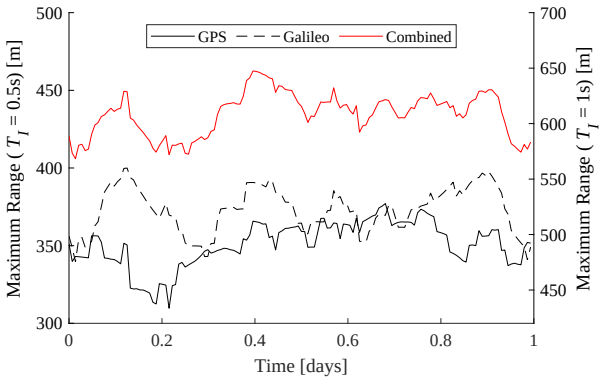

Fig. 6: Case Study II: Maximum detectable range achieved in BS configuration suing all the visible satellites in different constellations and a combination of both; left axis for integration time $T_I = 0.5$s and right axis for $T_I = 1$s.

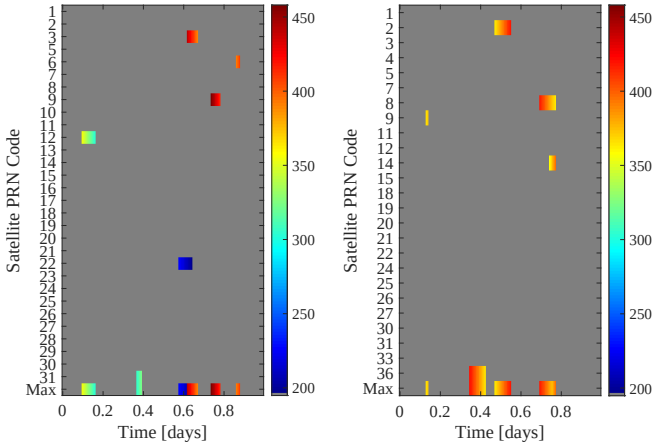

(a) GPS (b) Galileo

Fig. 7: Case Study II: Maximum detectable range [m] achieved in FS configuration using one satellite for detection.

To examine the FS-RCS only satellites positioned south of the airport, particularly between 250° and 270° azimuth angle, and between 5° and 50° elevation angle in TCS are considered. In Fig. 7 the maximum detectable range is shown to be achieved from each satellite using an integration time of $T_I = 0.1$s. Comparing Fig. 7 to Fig. 4, it can be seen that available satellites are much more sparse in Case Study II than Case Study I. Particularly, both GPS and Galileo will have non-zero range for only 26.4% of the day.

Considering both case studies, it can be seen that while the FS configuration can offer significantly higher detectable ranges when individual satellites are considered, the low availability of satellites in the desired configuration makes it unsuitable for most real-world applications. In the contrary, while BS configurations offer lower maximum range for individual satellites, the availability of the satellites is much higher. Additionally, non-coherent ingratiation of multiple satellites in BS can offer similar maximum ranges to the FS configuration, while if longer coherent integration in time, not available in FS, is considered the resulting ranges can be even higher. A combination of both configurations using two branches, one for BS which can stay always on-line and one for FS operating when available satellites are present, would be the most advantageous approach in terms of detection performance.

3 Proposed System

One of the basic operating principles of PBR systems is that the receiver shall have knowledge of the transmitted radar signal in order to apply correlation processing, also referred to as *matched filtering* or *pulse compression*, to improve the SNR and properly extract the target's parameters. Here the appropriate signal model and reconstruction algorithm derived in [19] are described.

3.1 Signal Model

The generic form of a GNSS signal transmitted by the i-th satellite is:

$$s_i(t) = m_i(t)g_i(t)e^{j2\pi f_0 t}; \tag{9}$$

where f_0 denotes the carrier frequency, $g_i(t)$ is a Pseudorandom Noise (PRN) code sequence and $m_i(t)$ is a navigation message. Examining the individual components, $g_i(t)$ is generated by repeating a Binary Phase Shift Keying (BPSK) modulated sequence composed of N_c chips, each of which has duration equal to T_c. Furthermore, the information carried by $m(t)$ is also coded using a BPSK modulation, with a symbol duration T_m which is significantly higher than T_c, i.e. $T_m \gg T_c$. Since the PRN code used by each satellite is known by the receiver, as it is used for the detection of the signal, it is useful to define its duration as the Pulse Repetition Interval (PRI) of the transmitter which equals to $\mathrm{PRI} = N_c T_c$. Based on this PRI, *fast-time* is defined as the time between the beginning and the end of each PRI, i.e. $t \in [0, \mathrm{PRI}]$, while intervals of a PRI, i.e. $u = 0, \mathrm{PRI}, 2\mathrm{PRI}, ...$ are referred to as *slow-time*.

Knowing that the transmitter-receiver channel changes in slow time and no propagation losses, the direct path signal from the i-th GNSS satellite at the passive receiver can be expressed in intermediate frequency as:

$$r_i(t,u) = m_i(u)g_i(t,u)e^{j[2\pi f_i(u)(t+u)+\phi_i(u)+\psi_i(u)]} \tag{10}$$

where τ_i, f_i and ϕ_i are the signal's time, frequency and phase shifts respectively caused due to the distance and relative velocity between the satellite and the receiver, and ψ_i is a phase error caused by non- free-space propagation phenomena such as hardware imperfections. Notice that since the channel varies in slow-time, the delay, frequency shift and phase error are modelled in slow-time. Furthermore, the different components are given as:

$$m_i(u) = m_i\big(\tau_i(u)\big) \tag{11}$$

$$g_i(t,u) = g_i\big(t - \tau_i(u)\big) \tag{12}$$

$$\phi_i(u) = 2\pi\big(f_0 + f_i(u)\big)\tau_i(u) \tag{13}$$

It is worth noting that since $T_m \gg T_c$, the navigation message $m_i(t)$ has also been modelled in slow time.

Based on (10), the return signal from a target is given as:

$$\hat{r}_i(t,u) = \hat{m}_i(t,u)\hat{g}_i(t,u)e^{j[2\pi \hat{f}_i(u)(t+u)+\hat{\phi}_i(u)+\hat{\psi}_i(u)]} \tag{14}$$

where $\hat{\tau}_i(u)$, $\hat{f}_i(u)$ and $\hat{\psi}_i(u)$ are the delay, frequency shift and phase error that the signal experiences in the satellite-target-receiver path. The parameters $\hat{m}_i(t,u)$, $\hat{g}_i(t,u)$ and $\hat{\phi}_i(u)$ can be calculated similarly to their counterparts for the direct path propagation, see (11), (12) and (13) respectively, by substituting $\tau_i(u)$ with $\hat{\tau}_i(u)$ and $f_i(u)$ with $\hat{f}_i(u)$.

3.2 GNSS Signal Parameters

In order to assess the performance of the proposed PBR configurations, the operating waveforms $g_i(t)$ shall be examined. A common tool for Radar waveform analysis is the *ambiguity function* (AF), which is a two dimensional function showing the response of a time and frequency shifted signal when a matched filter based on the reference signal is applied [28]. In Fig. 8a the AF of the space vehicle number (SVN) 1 GPS satellite signal is shown, overlaid by the zero-Doppler and zero-delay cuts. It should be noted that all the codes in one constellation exhibit similar AF and therefore examining only one example is sufficient for the current analysis. In Fig. 8b the AF of the SVN 1 Galileo satellite signal is shown. Comparing Fig. 8a and Fig. 8b it can be seen that both signals offer a "thumbtack" shaped AF with high response around the centre and low values elsewhere. This is significant for radar systems as it indicated proper localisation of the target and low ambiguities.

Under closer investigation, it can be seen that the Galileo signal offers finer Doppler resolution which is expected due to its longer duration. The AF parameters of the examined signals are summarised in Table 2. As it can be seen, the pulse repetition frequency of the GPS signal is 1kHz while for Galileo this valued drops by a factor of 4 due to its longer duration. As a consistence, GPS have higher unambiguous Doppler than Galileo. While the measured Doppler will depend on the geometry of the transmitter-receiver-target system [29], to place these number into perspective assume the case where the satellite is behind the receiver and the target is moving straight towards them. The experienced Doppler in this case is maximum and is given by:

$$f_{\mathrm{d,bi}} = \frac{2V_{\mathrm{g}}}{\lambda} \tag{15}$$

For $V_{\mathrm{g}} = 30$m/s the measured Doppler is 315Hz meaning that Galileo might exhibit Doppler ambiguities in such configurations. Lastly, the GPS and Galileo satellites offer the same range resolution, due to same bandwidth of their pulses.

3.3 Signal Reconstruction Algorithm

The adopted signal reconstruction algorithm is based on the synchronisation algorithm proposed in [10] with its basic operations being outlined in Fig. 9. The system utilises two channels: a reference channel used to capture the direct signals form the available satellites and a surveillance channel that captures the target's reflections.

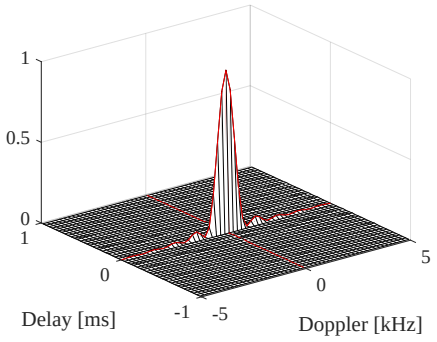

(a) GPS

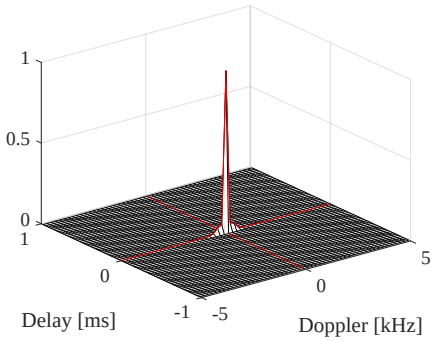

(b) Galileo

Fig. 8: Example AF of (a) GPS and (b) Galileo code signal

Table 2 Radar Parameters

	Description		GPS	Galileo
PRF	Pulse Repetition Frequency	[Hz]	1000	250
$f_{\mathrm{d,un}}$	Maximum unambiguous Doppler	[Hz]	500	125
ΔD	Range resolution	[m]	146.5	146.5

The input from the reference channel is passed through a standard GNSS receiver chain where the signals from different satellites are first detected by correlating the reference channel signal with different PRN sequences. This process is commonly referred to as *signal acquisition* and provides initial estimations regarding the code delay and Doppler shift of the signal. This information is later passed to a PRN code tracker which provides a finer and continuous estimation of the signal delay, Doppler and phase parameters. Based on these parameters, the reference signals from the different IOs can be reconstructed and correlated with the surveillance signal. The outputs of the different matched filters can be used for further radar processing.

Using the signal model derived in Section 3.1, the signal at the reference and surveillance channels can be expressed as:

$$r_R(t,u) = \sum_{i=1}^{N_i} \sqrt{a_{i,R}(u)} r_i(t,u) + \sum_{i=1}^{N_i} \sqrt{\hat{a}_{i,R}(u)} \hat{r}_i(t,u) + n_R(t,u) \quad (16)$$

$$r_S(t,u) = \sum_{i=1}^{N_i} \sqrt{a_{i,S}(u)} r_i(t,u) + \sum_{i=1}^{N_i} \sqrt{\hat{a}_{i,S}(u)} \hat{r}_i(t,u) + n_S(t,u) \quad (17)$$

where $a_{i,R}(u)$, $\hat{a}_{i,R}(u)$ represent the power losses in the reference channel owing to the satellite-receiver and satellite-target-receiver paths, and $a_{i,S}(u)$ and $\hat{a}_{i,S}(u)$ are the respective losses in the surveillance channel. If $a_{i,R}(u) \gg \hat{a}_{i,R}(u)$ is satisfied, the tracker can provide an estimate of the delay $\tilde{\tau}_i(u) \approx \tau_i(u)$, frequency shift $\tilde{f}_i(u) \approx f_i(u)$ and phase shift $\tilde{\phi}_i(u) \approx \phi_i(u)$ that the signal experiences in the satellite-receiver path. Additionally, the tracker outputs an estimate of the navigation signal $\tilde{m}_i(u)$ containing binary phase information. Using these estimates, the signal from the i-th satellite can be reconstructed as:

$$\tilde{r}_{i,D}(t,u) = \tilde{m}_i(u)\tilde{g}_i(t,u)e^{j[2\pi\tilde{f}_i(u)(t+u)+\tilde{\phi}_i(u)]} \quad (18)$$

where $\tilde{g}_i(t,u) = g_i\big(t - \tilde{\tau}_i(u)\big)$ is the time shifted PRN code.

After the different satellite signals in (18) have been reconstructed, they can be used to filter the signal from the surveillance channel. By design, the signals transmitted from different satellites are near orthogonal, thus the cross-correlation between the reconstructed signal (18) and the surveillance channel (17) can be expressed as:

$$Y_i(k,u) = \int_0^{\mathrm{PRI}} \tilde{r}_{i,D}^{\dagger}(t-k,u) r_S(t,u)\mathrm{d}t \quad (19)$$

$$= y_i(k,u) + \hat{y}_i(k,u) + n_i(k,u) \quad (20)$$

where $(\cdot)^{\dagger}$ denotes the complex conjugate operation, and $y_i(k,u)$, $\hat{y}_i(k,u)$, $n_i(k,u)$ are the correlation output components associated with the direct signal, target returns and noise respectively. For an accurate reconstruction of the signal, and if the phase error in both channels is approximately the same, i.e. $\tilde{\psi}_i(u) \approx \psi_i(u)$, $y_i(k,u)$ and $\hat{y}_i(k,u)$ can be expressed as [19]:

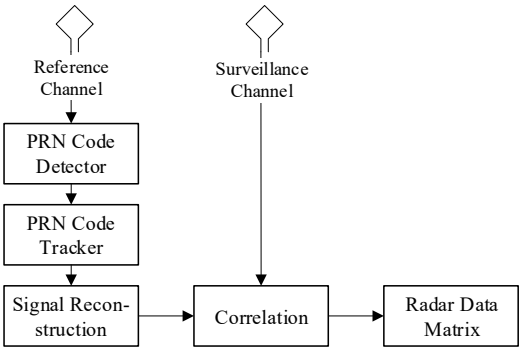

Fig. 9: Signal reconstruction algorithm.

$$y_i(k,u) = \sqrt{a_{i,S}(u)}\mathcal{A}(k,0) \quad (21)$$

$$\hat{y}_i(k,u) = \sqrt{\hat{a}_{i,S}(u)}\mathcal{A}(\Delta\tau_i(u)+k, \Delta f_i(u)) \quad (22)$$

where $\mathcal{A}(\tau, f)$ is the AF of the PRN code at a delay τ and frequency shift f, and $\Delta\tau_i(u) = \tau_i(u) - \tilde{\tau}_i(u)$ and $\Delta f_i(u) = f_i(u) - \tilde{f}_i(u)$ represent the bi-static delay and Doppler shift respectively. From (21) and (22) it can be seen that the output from the filtered signal $Y_i(k,u)$ comprises two main components: one at zero-delay and zero-Doppler and one at $\Delta\tau_i(u)$ and $\Delta f_i(u)$. If $\Delta\tau_i(u) \neq 0$ or $\Delta f_i(u) \neq 0$ it is therefore possible to estimate the target's range and velocity after filtering the direct signal component. In the literature, various direct signal suppression techniques have been proposed. As this issue remains out of the scope of this research, the reader is referred to [29, 30] for further discussion.

4 Target Parameters Estimation

Two of the primary parameters that a radar system shall be able to estimate after detecting a target is its position and velocity. Having knowledge of the transmitter's position and relative velocity, the measured bistatic range and Doppler derived from the delay and frequency shift experienced in the surveillance channel can be converted respectively to range from the receiver and velocity in the bisector of the bistatic angle θ [29]. In the case of FS, setting the bistatic angle $\theta = 180^{\circ}$ results in infinite range resolution and 0 Doppler shift. While this might be the case for the target crossing the baseline between the transmitter and receiver, in near baseline configuration, frequency modulation is still apparent. This phenomenon was extensively investigated in [17] where a bank of filters, designed based on the envelope and Doppler signature that a target will impose under different range and velocity configurations, was used for detection and range and velocity estimation. In this paper, the target localisation problem is dealt with by employing a MISO approach. This allows to utilise the return from multiple satellites and exploit their spatial diversity. It should be noted that the proposed approach does not address the FS case, however since such methods have already been presented in the literature they remain out of the scope of this work and will not be discussed in this section. The reader is advised to refer to [17] for further discussion in FS localisation techniques.

4.1 Location estimation

Assuming the acquisition of one PRI in the presence of a target we define r_i as the $N \times 1$ vector containing the discrete samples of the signal transmitted by the i-th satellite, reflected by the target and captured at the receiver. The total received signal can be defined as:

$$r = \sum_{i=1}^{N_i} r_i + n \quad (23)$$

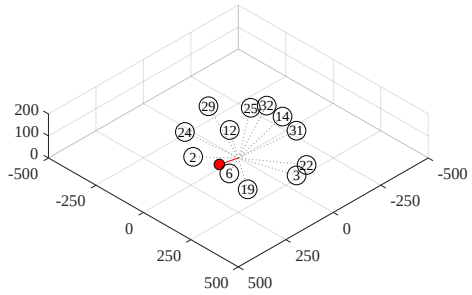

Fig. 10: Examined geometry with the receiver placed at $(0, 0, 0)$, the coordinated of each satellite being scaled down and the target denoted by the red dot.

where N_i is the number of available satellites and n is additive white Gaussian noise. Accounting for zero-Doppler form the target in fast-time, the MISO AF of the received signal is defined as:

$$A_{\mathrm{Co}}(x, y, z) = \sum_{i=1}^{N_i} r_i^{\dagger}(x, y, z) r \tag{24}$$

where x, y and z are the spatial parameters in a X-Y-Z three dimensional space, $r_i(x, y, z)$ is the expected signal from a target in the (x, y, z) coordinates associated with the i-th satellite, and $(\cdot)^{\dagger}$ is the complex conjugate operation. It is worth mentioning that here a perfect reconstruction of the satellite signal is assumed, meaning that delay and Doppler shifts due to the satellite position and motion are accounted in $r_i^{\dagger}(x, y, z)$. Examining (24), it can be easily seen that the MISO AF is defined as the coherent sum of the AFs for the different satellite signals $A_{\mathrm{i}}(x, y, z)$, i.e.:

$$A_{\mathrm{Co}}(x, y, z) = \sum_{i=1}^{N_i} A_i(x, y, z) \tag{25}$$

This process can be considered as synthesising a large multi-element transmitter array using all the satellites. While coherently processing all the returns can singularity improve the localisation of the target, it will be very sensitive to phase mismatch. To mitigate this issue, the AFs from the different satellites can be added non-coherently:

$$A_{\mathrm{In}}(x, y, z) = \sum_{i=1}^{N_i} |A_{\mathrm{i}}(x, y, z)| \tag{26}$$

This method avoids the high phase sensitivity that coherent MISO AF suffers from, offering however degraded localisation perforce as phase information are not considered. As mentioned in Section 2.2, since coherency between the different satellite signals might not be achievable in most cases, non-coherent integration will be adopted when combining the different AFs.

For a better understanding of the system's behaviour, consider the following simplified example. Assume a source placed at the Heathrow airport and the configuration of the available GPS satellites shown in Fig. 10. A target is placed at the surveillance area with the received signal being modelled based on Section 3 assuming perfect reconstruction. To calculate the reflected target's power received from each satellite, (3) is used by replacing P_n with 1. Furthermore, no noise is assumed while the in-between samples delays are modelled using fractional delay by linear interpolation [31]. In Fig. 8 the X-Y cross-sections of the non-coherent MISO AF is show for $z = 20$m and the target placed at different positions. Each MISO AF is normalised by its maximum value the bin step in all dimensions is 10m starting form -500m up to 500m in X and Y axis and 0m to 250m in Z. As it can be seen the response of the MISO AF is highly dependent on the targets position. Particularly, when the target is placed away from the receiver, see Fig. 11a and Fig. 11c, the response appears similar to an arc while when placed on top of the receiver it is more similar to a circle. Furthermore, when there is a mismatch in height, see Fig.11d the response has lower intensity.

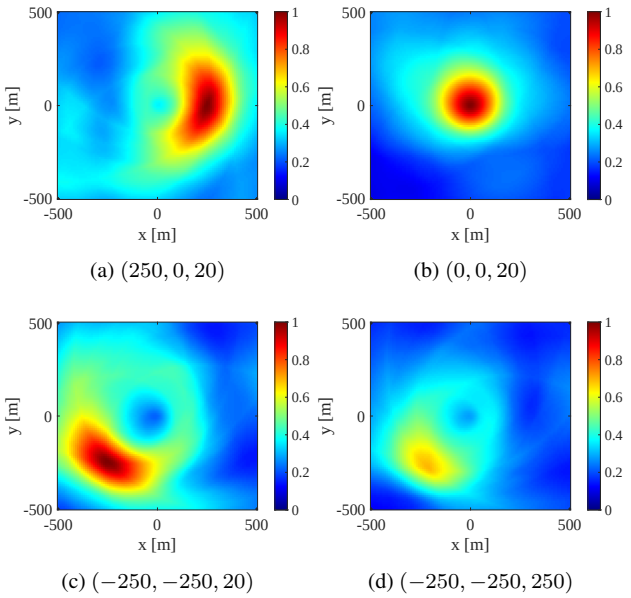

(a) $(250, 0, 20)$ (b) $(0, 0, 20)$

(c) $(-250, -250, 20)$ (d) $(-250, -250, 250)$

Fig. 11: MISO AF coss-section at $z = 20$m for different target position and the receiver satellite topology shown in Fig.10

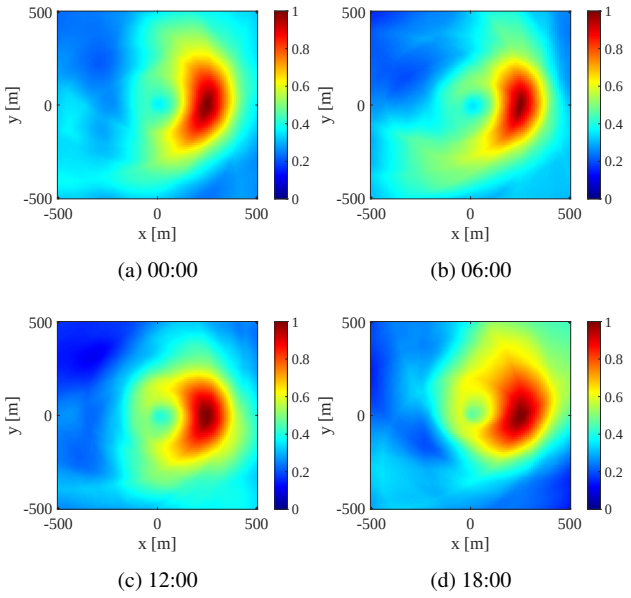

(a) 00:00 (b) 06:00

(c) 12:00 (d) 18:00

Fig. 12: MISO AF coss-section at $z = 20$m for the target placed at $(250, 0, 20)$ at different hours of the day.

To access the performance of during different parts of the day, Fig.12 show the MISO AF of the target when placed at $(250, 0, 20)$ at different hours of the day. As it can be seen, for different time the response changes due to the different satellites position. It is also worth noting that the spatial resolution in the radial direction is not constant and higher than the one described in Table 2. This is caused due to the bistatic resolution in the different AFs A_i varying based on the respective bistatic angle θ.

4.2 Doppler Processing

The Doppler introduced by the UAV is assumed to be a slow time phenomenon. That means that the reflected fast time signal will exhibit a frequency shift only caused by the satellite relative motion and the current geometry. Moreover, the target's Doppler is translated in different phase shifts observed in slow time. Therefore, the formula of MISO AFs derived in (26) are not sufficient in order to estimate the target's velocity. In monostatic and bistatic configurations the Doppler processing usually involves a Fourier Transform across the slow time samples of each fast time bin. As in MISO the Doppler experienced from different transmitter-receiver pairs cannot be converted to velocity along the same axis, similar to the displacement the velocity is estimated along all three X-Y-Z axes. Extending (26) under the assumption of slow time processing results in:

$$A_{\mathrm{In}}(x,y,z,v_x,v_y,v_z,m_0) = \sum_{i=1}^{N_i}\left|\sum_{m=1}^{N_c} r_i^{\dagger}(x,y,z)r(m+m_0)e^{-2\pi f_{D,i}(v_x,v_y,v_z)m}\right| \quad (27)$$

where v_x, v_y and v_z denote the velocity in the different axis, m_0 is the starting slow time sample of the examined interval, N_c is the number of slow time samples composing a coherent time interval (CPI), m is the index of the slow time samples, and $f_{D,i}(v_x,v_y,v_z)$ is the expected bistatic Doppler in the i-th satellite signal divided by the PRF.

5 Micro-Doppler in GNSS PBR

As discussed in Section 4.2, the velocity characteristics of a target can be extracted by applying frequency analysis through a CPI. Along with information about its moving direction and speed, the main Doppler of the target can be used to discriminate it from strong reflections due to stationary clatter in the scene. One of the main issue with UAV targets however, is that their velocity characteristics can be very similar to those of no-stationary clutter such as trees and birds. For this reason *micro-Doppler* analysis has been generally proposed for UAV monitoring solutions [21].

In radar systems, micro-Doppler refers to the frequency shifts on the received signal due to the targets secondary motions [32]. For UAV targets specifically, the rotor blades motion is the main source of micro-Doppler signatures [21]. This results to a very unique time-frequency signature that can be used to separate then from other targets. In [33] a general signal model for UAV micro-Doppler was discussed. Here, the same framework is employed to investigate the feasibility of micro-Doppler signature extraction using GNSS based PBR. Additionally, a bird target will be considered following the kinematic model proposed in [32]. Section 4.1 described the scenario of a receiver placed at the Heathrow airport with the configuration of the available GPS satellites shown in Fig. 10. The receiver is set at the centre of the co-ordinate system, with the target's centre of mass is considered static at $(100, 0, 20)$ in X-Y-Z coordinates. The different parameters for the UAV and bird targets are summarised in Table 3 while their models are shown in Fig. 13. Particularly, the UAV target comprises 4 two-side rotating blades, or 8 one-side blades each of them simulated as a unitary RCS scatterer at the tip of the blade (see dots in Fig. 13a). It should be noted that the rest of the UAV's body is not considered as no other parts exhibit different motions than the centre of mass. Furthermore, the bird target comprises 2 scatterers for each wing and 3 scatterers for the torso, giving in total 7 scatters (see dots in Fig. 13b and 13c).

In Fig.14 the spectrograms of the two targets are shown using satellite No.14 as illuminator, giving a bistatic angle of $\theta = 55^{\circ}$, and a $T_w = 0.3$s window. Comparing the two spectrograms, it can be seen that the two targets exhibit very different micro-Doppler profiles. Specifically, when a window much longer than the rotation period of the rotors, $T_w > 1/\Omega$, is used, the spectrogram of the UAV is characterised by parallel frequency components. On the other hand, since the flapping period of the bird is significantly longer than the rotation of the blades, the different frequency fluctuations due to the individual scatterers can be extracted for the same window, $T_w < 1/f_f$. Additionally, due to much faster motion of the UAV target's blades, aliasing is present in Fig.14a. In comparison, the bird target in Fig.14b exhibits significantly lower frequency shifts. It should be noted that while in both cases $\mathrm{PRF} = 1$kHz (see Table .2), different frequency axes have been used for the two spectrograms for better illustration. These results can also be validated by comparing them with the experimental acquisitions demonstrated in [34], where similar behaviour can be observed. These different characteristics can therefore be exploited by the proposed GNSS PBR system for target discrimination. It is worth noting that while here an analysis on the returns from only one satellite is considered, mutlistatic approaches for micro-Doppler based UAV detection and tracking have been proposed in the literature [35]. Similar approaches could be used from the proposed system to exploit multiple returns from the different satellites.

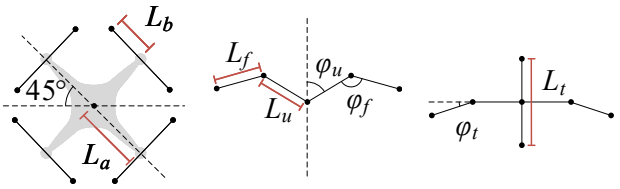

(a) UAV top (b) Bird front (c) Bird top

Fig. 13: Models of examined targets: (a) UAV top view, (b) bird front view and (c) bird top view.

Table 3 Target Parameters

UAV Parameter			
Blade length	L_b	120	mm
Arm length	L_a	175	mm
Rotation speed of blades	Ω	733	rad/s
Number of rotors	M	4	
Number of UAV scatterers		8	
Bird Parameter			
Body length	L_t	0.8	m
Upper arm length	L_u	0.5	m
Forearm length	L_f	0.5	m
Flapping frequency	f_f	1	flaps/s
Upper arm angle	ϕ_u	$[-25, 55]$	deg
Forearm flapping angle	ϕ_f	$[-10, 70]$	deg
Forearm twist angle	ϕ_t	$[-20, 20]$	deg
Number of bird scatterers		7	

6 Conclusion

The paper presented a feasibility study of UAV monitoring using GNSS based PBR systems. Particularly, an estimate of the maximum detectable range for small UAV targets was investigated along with the availability of illuminators under back and forward scattering assumptions. Using two different case studies, it was shown that Galileo satellites can offer higher maximum ranges compared to GPS. Additionally, using all the satellites in one constellation guaranties persistent 24-hour availability in BS configuration, while using all the available satellites offers longer detectable ranges. Examining the FS performance for certain orientations, it was demonstrated that while FS-RCS can offer longer maximum detectable range than BS-RCS, the availability of the satellites in FS configuration is quite sparse. The design of the proposed system was derived, describing the appropriate signal model and signal

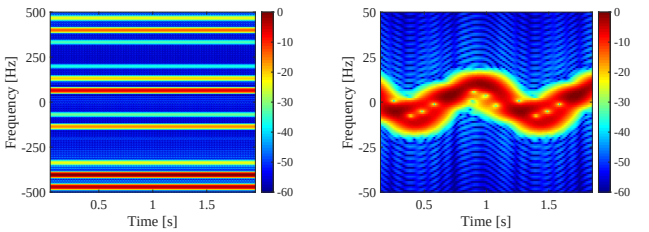

(a) UAV (b) Bird

Fig. 14: Spectrograms of (a) UAV and (b) bird target using a 0.1s Hamming window.

reconstruction algorithm necessary to perform correlation operations. Furthermore, in order to estimate the target's location and velocity a MISO approach using non-coherent integration of different satellite returns was proposed. The behaviour of the MISO AF was investigated under different target position and part of the day scenarios. Finally, a comparison between a UAV and bird target was presented based on simulated time-frequency profiles. Results demonstrated the capability of the proposed GNSS PBR system to exploit the micro-Doppler signatures of the different targets for discrimination.

7 References

1 M. A. Richards, J. A. Scheer, W. A. Holm, B. Beckley, P. Mark, A. Richards *et al.*, "Principles of Modern Radar Volume I-Basic Principles," 2010.

2 Y. Liu, X. Wan, H. Tang, J. Yi, Y. Cheng, and X. Zhang, "Digital television based passive bistatic radar system for drone detection," in *2017 IEEE Radar Conference (RadarConf)*, May 2017, pp. 1493–1497.

3 C. Schüpbach, C. Patry, F. Maasdorp, U. Böniger, and P. Wellig, "Micro-UAV detection using DAB-based passive radar," in *2017 IEEE Radar Conference (RadarConf)*, May 2017, pp. 1037–1040.

4 B. Knoedler, R. Zemmari, and W. Koch, "On the detection of small UAV using a GSM passive coherent location system," in *2016 17th International Radar Symposium (IRS)*, May 2016, pp. 1–4.

5 C. Clemente and J. J. Soraghan, "Passive bistatic radar for helicopters classification: A feasibility study," in *2012 IEEE Radar Conference*, May 2012, pp. 0946–0949.

6 C. Clemente and J. J. Soraghan, "GNSS-Based Passive Bistatic Radar for Micro-Doppler Analysis of Helicopter Rotor Blades," *IEEE Transactions on Aerospace and Electronic Systems*, vol. 50, no. 1, pp. 491–500, January 2014.

7 C. Clemente, T. Parry, G. Galston, P. Hammond, C. Berry, C. Ilioudis, D. Gaglione, and J. J. Soraghan, "GNSS based passive bistatic radar for micro-Doppler based classification of helicopters: Experimental validation," in *2015 IEEE Radar Conference (RadarCon)*, May 2015, pp. 1104–1108.

8 C. Liu, C. Hu, R. Wang, X. Nie, and F. Liu, "GNSS forward scatter radar detection: Signal processing and experiment," in *2017 18th International Radar Symposium (IRS)*, June 2017, pp. 1–9.

9 A. D. Luca, L. Daniel, M. Gashinova, and M. Cherniakov, "Target parameter estimation in moving transmitter moving receiver forward scatter radar," in *2017 18th International Radar Symposium (IRS)*, June 2017, pp. 1–7.

10 M. Antoniou and M. Cherniakov, "GNSS-based bistatic SAR: a signal processing view," *EURASIP Journal on Advances in Signal Processing*, vol. 2013, no. 1, p. 98, May 2013.

11 H. Ma, M. Antoniou, M. Cherniakov, D. Pastina, F. Santi, F. Pieralice, and M. Bucciarelli, "Maritime target detection using GNSS-based radar: Experimental proof of concept," in *2017 IEEE Radar Conference (RadarConf)*, May 2017, pp. 0464–0469.

12 A. D. Chadwick, "Micro-drone detection using software-defined 3G passive radar," in *International Conference on Radar Systems (Radar 2017)*, Oct 2017, pp. 1–6.

13 M. P. Jarabo-Amores, D. Mata-Moya, P. J. Gomez-del-Hoyo, J. L. Barcena-Humanes, J. Rosado-Sanz, N. Rey-Maestre, and M. Rosa-Zurera, "Drone detection feasibility with passive radars," in *2018 15th European Radar Conference (EuRAD)*, Sep. 2018, pp. 313–316.

14 P. Addabbo, G. Giangregorio, C. Galdi, and M. di Bisceglie, "Simulation of TechDemoSat-1 Delay-Doppler Maps for GPS Ocean Reflectometry," *IEEE Journal of Selected Topics in Applied Earth Observations and Remote Sensing*, vol. 10, no. 9, pp. 4256–4268, Sep. 2017.

15 S. L. Ullo, G. Giangregorio, M. di Bisceglie, C. Galdi, M. P. Clarizia, and P. Addabbo, "Analysis of GPS signals backscattered from a target on the sea surface," in *2017 IEEE International Geoscience and Remote Sensing Symposium (IGARSS)*, July 2017, pp. 2062–2065.

16 Y. Wu, W. Qu, H. Wang, X. Jia, and S. Ji-liang, "Study on bistatic (multi) radar system using navigation satellites," in *2008 8th International Symposium on Antennas, Propagation and EM Theory*, Nov 2008, pp. 1286–1289.

17 N. Ustalli, F. Di Lello, D. Pastina, C. Bongioanni, S. Rainaldi, and P. Lombardo, "Two-dimensional filter bank design for velocity estimation in forward scatter radar configuration," in *2017 18th International Radar Symposium (IRS)*, June 2017, pp. 1–10.

18 N. Ustalli, D. Pastina, and P. Lombardo, "Target motion parameters estimation in forward scatter radar," *IEEE Transactions on Aerospace and Electronic Systems*, pp. 1–1, 2019.

19 C. Ilioudis, J. Cao, I. Theodorou, P. Striano, W. Coventry, C. Clemente, and J. Soraghan, "GNSS based passive radar for UAV monitoring," in *IEEE Radar Conference 2019*, April 2019.

20 N. J. Willis, *Bistatic radar*. SciTech Publishing, 2005, vol. 2.

21 J. S. Patel, F. Fioranelli, and D. Anderson, "Review of radar classification and rcs characterisation techniques for small uavs or drones," *IET Radar, Sonar Navigation*, vol. 12, no. 9, pp. 911–919, 2018.

22 S. Rzewuski, K. Kulpa, B. Salski, P. Kopyt, K. Borowiec, M. Malanowski, and P. Samczyński, "Drone RCS estimation using simple experimental measurement in the WIFI bands," in *2018 22nd International Microwave and Radar Conference (MIKON)*, May 2018, pp. 695–698.

23 M. Gashinova, L. Daniel, E. Hoare, V. Sizov, K. Kabakchiev, and M. Cherniakov, "Signal characterisation and processing in the forward scatter mode of bistatic passive coherent location systems," *EURASIP Journal on Advances in Signal Processing*, vol. 2013, no. 1, p. 36, 2013.

24 M. Skolnik, *Radar Handbook, Third Edition*, ser. Electronics electrical engineering. McGraw-Hill Education, 2008.

25 A. R. Persico, P. Kirkland, C. Clemente, M. Vasile, and J. J. Soraghan, "Cubesat-based passive bistatic radar for space situational awareness: A feasibility study," *IEEE Transactions on Aerospace and Electronic Systems*, pp. 1–1, 2018.

26 P. Steigenberger, S. Thoelert, and O. Montenbruck, "GNSS satellite transmit power and its impact on orbit determination," *Journal of Geodesy*, vol. 92, no. 6, pp. 609–624, Jun 2018.

27 C. Rino, "Satellite orbit computation," 2010, uk.mathworks.com/ matlabcentral/ fileexchange/ 28888-satellite-orbit-computation.

28 P. M. Woodward, *Probability and Information Theory, with Applications to Radar: International Series of Monographs on Electronics and Instrumentation*. Elsevier, 2014, vol. 3.

29 H. D. Griffiths and C. J. Baker, *An introduction to passive radar*. Artech House, 2017.

30 J. L. Garry, G. E. Smith, and C. J. Baker, "Direct signal suppression schemes for passive radar," in *2015 Signal Processing Symposium (SPSympo)*, June 2015, pp. 1–5.

31 Mathworks, "Variable fractional delay," 2019, uk.mathworks.com/ help/ dsp/ ref/ variablefractionaldelay.html.

32 V. C. Chen, *The micro-Doppler effect in radar*. Artech House, 2019.

33 C. Ilioudis, C. Clemente, and J. Soraghan, "Understanding the potential of self-protection jamming on board of miniature uavs," in *Internationa Radar Conference 2019 (Radar 2019)*, April 2019.

34 M. Ritchie, F. Fioranelli, H. Griffiths, and B. Torvik, "Monostatic and bistatic radar measurements of birds and micro-drone," in *2016 IEEE Radar Conference (RadarConf)*, May 2016, pp. 1–5.

35 F. Hoffmann, M. Ritchie, F. Fioranelli, A. Charlish, and H. Griffiths, "Micro-doppler based detection and tracking of uavs with multistatic radar," in *2016 IEEE Radar Conference (RadarConf)*, May 2016, pp. 1–6.